

Navigating entanglement via Ruderman-Kittel-Kasuya-Yosida exchange: Oscillatory, boundary-residing, pulsed, and damping-stabilized trajectories

Son-Hsien Chen ,^{1,*} Seng Ghee Tan ,² and Ching-Ray Chang ,³

¹*Department of Applied Physics and Chemistry, University of Taipei, Taipei 100234, Taiwan*

²*Department of Optoelectric Physics, Chinese Culture University, Taipei 11114, Taiwan*

³*Quantum Information Center, Chung Yuan Christian University, Taoyuan, 320314, Taiwan*

(Dated: January 1, 2026)

Entanglement dynamics are fundamental to quantum technologies, yet controlling their temporal evolution in a reversible and stable manner remains challenging. We propose a solid-state framework based on the Ruderman-Kittel-Kasuya-Yosida interaction, realizable in gate-defined quantum dots or suspended structures, in which two spin qubits couple to a central spin qudit that mediates an effective, time-dependent exchange. The dynamics are governed by an exchange-time integral that unifies interaction strength and physical time into a single scalar control variable, enabling *time-reversible* and cyclic navigation of the Hilbert space. Crucially, we show that out-of-phase modulation grants access to higher entanglement subspaces, while introducing damping to the exchange modulation achieves stabilized trajectories that drive the system toward stationary entanglement values. This framework provides a systematic route for shaping entanglement dynamics, particularly in the *near-boundary regime*, using exchange control alone, overcoming the limitations of monotonic evolution and offering practical strategies for entanglement stabilization in realistic solid-state architectures, with direct relevance to quantum metrology and environment-assisted entanglement engineering.

I. INTRODUCTION

Quantum entanglement refers to the nonclassical correlations between subsystems, where the overall quantum state cannot be factored into independent states of the individual parts [1, 2]. This correlation plays a pivotal role in emerging quantum technologies [3], underpinning advances in gravitational wave detection [4, 5], quantum cryptography [6–9], and quantum computation [2, 10–15]. Despite its foundational importance, entanglement generation and the control of its dynamics remain central challenges in quantum information science [16–19].

To address these challenges, diverse quantum processor platforms have been developed, including superconducting circuits [20], trapped ions [21, 22], and photonic qubits [23]. Among these, spin qubits in solid-state systems are particularly promising candidates, specifically those based on magnetic impurities or defect centers (e.g., nitrogen-vacancy centers in diamond, donor spins in silicon) and lithographically or gate-defined quantum dots (QDs). Defect-based qubits combine optical initialization and readout with long coherence times, enabling remote entanglement over distances of up to two meters [24]. Donor spins in silicon achieve coherence times on the order of seconds with gate fidelities above 99% [25–27], whereas QD spin qubits support dense integration and fast all-electrical control, with resonant CNOT gate fidelities above 98% [28–31]. Both architectures allow electrically tunable exchange coupling for rapid two-qubit gates and coherence protection via dynamical decoupling [30, 32]. This gate-voltage tunability enables adjustment of the final entanglement over a broad

range of strengths [33, 34].

However, realizing a scalable architecture with these spin qubits requires a robust long-range coupling mechanism, as direct exchange interaction is limited to nearest neighbors. To this end, both QDs [35–41] and magnetic impurities [42–45] can couple via Ruderman-Kittel-Kasuya-Yosida (RKKY) exchange [46–48]. This interaction is mediated by the host electrons, alternating between ferromagnetic and antiferromagnetic regimes with distance, which facilitates entanglement generation [43, 49], even at long range [37, 50].

Environment-mediated entanglement, such as that induced by RKKY, exhibits distinctive temporal behavior. It can change abruptly, leading to entanglement sudden death (ESD) [51–55]—a complete loss of entanglement in finite time—and its counterpart, entanglement sudden birth (ESB) [33, 56, 57]. These phenomena, observed in various solid-state [33, 57, 58] and optical systems [59], involve ESD-ESB transitions that can be of finite (TFD) or zero duration (TZD). The parity of the mediator [60, 61] critically determines the resulting entanglement. Furthermore, because entanglement reduces spin purity [62], accurately modeling these systems requires a fully quantum treatment, as semiclassical approaches (like the Landau-Lifshitz-Gilbert equation) fail to capture the non-conservation of local spin magnitude [63, 64].

Enhancing the tunability of entanglement often involves enabling qubit motion. Moving qubits have been explored in cavity quantum electrodynamics systems, where atoms coupled to cavity photons preserve entanglement by tuning their velocities [65–67] or prevent ESD by manipulating cavity-cavity interactions [68]. In the solid state, strong entanglement can be created by scattering ballistic electrons off magnetic impurities [69, 70]. However, a systematic and programmable method for shap-

* sonhsien@utaipei.edu.tw

ing the temporal entanglement profile—or trajectory—in solid-state systems is still lacking. Resolving this is of fundamental and practical significance for sustained entanglement distribution and the exploration of the dynamically accessible Hilbert space.

In this paper, we present an RKKY-exchange-based device for the systematic shaping of entanglement trajectories. The spin qubits considered here can be implemented using suspended impurity/defect centers or stationary QD-confined spins coupled effectively through the mediating two-dimensional electron gas (2DEG). We show that the dynamics are parameterized by the exchange-time integral (ETI), which acts as an effective evolution variable and enables the reversal of previously visited states along a trajectory. In our implementation, the required time dependence of the sign change in the exchange coupling is achieved by a motion-driven scheme (prescribing the spatial vibrational motion of the qubits). Alternatively, a gate-driven scheme, which switches the exchange between ferromagnetic and antiferromagnetic regimes via dynamical voltages $V_G(t)$ [44, 71, 72], can realize the same exchange dynamics without motion. We demonstrate that distinct trajectories can be achieved by employing the boundary-proximal initial states (ISs) identified through our recent work in Ref. 58, which are valuable for quantum metrology due to their sensitivity to external fields [73]. Furthermore, introducing damping to the out-of-phase vibrations facilitates the generation and stabilization of large entanglement. The proposed device enables reversible access to quantum states and supports applications exploiting near-boundary physics, characterized by weak entanglement. Moreover, by alternating the exchange polarity, our platform also offers an echo-like correction mechanism [32, 74], unwinding phase accumulation to mitigate dephasing.

The paper is organized as follows. Section II introduces the model, describes the device, and outlines the ISs required to realize ESD, ESB, and TFD. The subsequent numerical analysis is divided into two distinguishable dynamic regimes based on the boundedness of the exchange-time-integral (ETI). Section III A demonstrates cyclic navigation via in-phase and antiphase vibrations, where the system periodically retraces its path. In contrast, Section III B examines stabilized navigation, showing how out-of-phase modulation accesses higher entanglement subspaces while damping locks the system to a stationary entanglement value. Finally, Sec. IV summarizes our findings.

II. MODEL AND FORMALISM

In this section, we delineate the device architecture, establish the theoretical framework for the system, and introduce the ETI as the governing control variable. We then define the specific boundary-proximal ISs used to investigate the entanglement dynamics.

A. Hamiltonian and dynamics

As illustrated in Fig. 1(a), the proposed device consists of two spin qubits, A and B , separated by a distance $2R$, and a mediating environment. This environment comprises a central spin qudit C (a d -level spin- \vec{S}^C quantum system with spin \vec{S}^C) and the itinerant electrons of a 2DEG, denoted as e . The central spin polarizes the 2DEG, generating a spin-density imbalance whose sign oscillates with distance—a hallmark of the RKKY interaction. We examine the entanglement between the two qubits mediated by this exchange. Coupling to the environment can be realized via two schemes: (i) suspended qubits interacting with local electron spins in the 2DEG via proximity effects [Fig. 1(a)], or (ii) stationary qubits confined by QDs in the 2DEG [Fig. 1(b)]. Since both schemes generate equivalent sign-alternating exchange (the latter via dynamical gate voltages [44, 71, 72]), we will focus our analysis on the case of suspended qubits.

The local s - d exchange interaction between the spins (qubits or qudits) and the conduction electrons is modeled using a Dirac delta function as

$$H_{sd} = J_{sd} \sum_{i \in \{A, B, C\}} \vec{S}^i \cdot \vec{\sigma}^e \delta(\vec{r}^e - \vec{r}^i), \quad (1)$$

which, upon integrating out the electron degrees of freedom, yields an effective indirect RKKY interaction among the localized spins:

$$\begin{aligned} H_{\text{RKKY}} = & J(r^{AB}) \vec{\sigma}^A \cdot \vec{\sigma}^B \\ & + J(r^{AC}) \vec{\sigma}^A \cdot \vec{S}^C \\ & + J(r^{BC}) \vec{\sigma}^B \cdot \vec{S}^C, \end{aligned} \quad (2)$$

where $\vec{r}^{ij} = \vec{r}^i - \vec{r}^j$. Here, \vec{r}^A , \vec{r}^B , \vec{r}^C , and \vec{r}^e denote the position vectors of qubits A and B , qudit C , and the electron, respectively. The operators $\vec{\sigma}^A$ and $\vec{\sigma}^B$ represent the Pauli vector matrices of the qubit subsystems, while \vec{S}^C is the spin operator of qudit C (where $\vec{S}^C = \vec{\sigma}^C/2$ for the $d = 2$ case). Notably, the coupling strength scales as $J(r) \propto J_{sd}^2$ and, in α spatial dimensions, decays as $J(r) \propto 1/r^\alpha$ (modulated by oscillations). Consequently, we neglect the direct coupling between A and B , assuming $J(r^{AB}) \ll J(r^{AC})$ and $J(r^{AB}) \ll J(r^{BC})$. The qubits are subject to a local, spin-independent orbital confinement potential H_o . The resulting spatial evolution $r^{AB}(t)$ governed by H_o leads to an effective spin Hamiltonian of the form

$$H = J(r^A(t)) \vec{\sigma}^A \cdot \vec{S}^C + J(r^B(t)) \vec{\sigma}^B \cdot \vec{S}^C, \quad (3)$$

where we have set the origin at $\vec{r}^C \equiv 0$. The explicit time dependence of the RKKY exchange terms, $J(r^A(t))$ and $J(r^B(t))$, originates from the motion of the qubits. This dependence can be induced by a simple harmonic confinement potential,

$$H_o = \frac{1}{2} k^A \left(\vec{r}^A - \vec{R}_0^A \right)^2 + \frac{1}{2} k^B \left(\vec{r}^B - \vec{R}_0^B \right)^2, \quad (4)$$

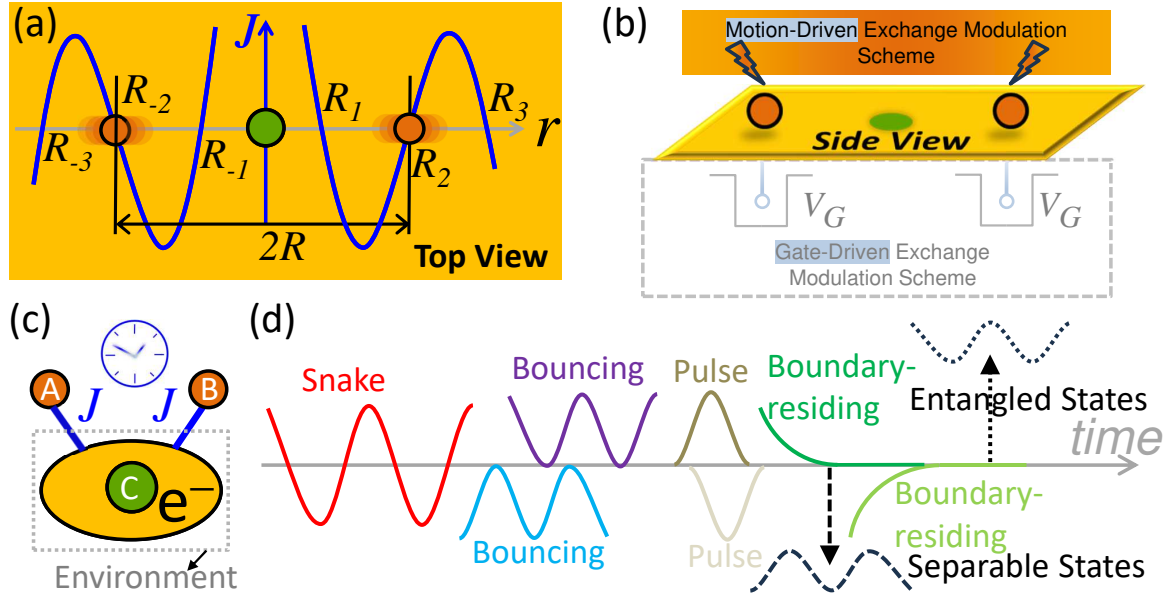


FIG. 1. System schematic and entanglement dynamics. (a) Top view of suspended spin qubits A and B (orange) coupled via an effective, alternating RKKY exchange J to a central spin qudit C (green). This coupling is mediated by the interaction between the qubits and the local electron spin polarization induced by the central qudit. The environment comprises C and a two-dimensional electron gas e (2DEG, yellow), and the spatial RKKY profile (blue) defines the exchange nodes R_n . (b) Side view illustrating the motion-driven exchange modulation scheme. Here, the exchange coupling to the underlying local electron spins is modulated by the distance between the qubits and the e -spins (non-contact proximity). Alternatively, a gate-driven scheme (gray dashed box), using an applied dynamical voltage $V_G = V_G(t)$, can generate an equivalent sign-alternating exchange interaction; in this scheme, stationary spins are confined within the V_G -defined quantum dots. (c) Conceptual illustration of the environment (gray dotted box) and the qubits. The Exchange-Time-Integral (ETI)—combining the exchange modulation (blue lines) and time (blue clock icon)—serves as the effective control parameter that determines the qubit evolution along a trajectory in Hilbert space. (d) Schematic representation of entanglement trajectories, where the horizontal gray line denotes the boundary separating the entangled (upper) and separable (lower) subspaces, highlighting distinct dynamical regimes including snake, bouncing, pulse, and boundary-residing trajectories.

which drives the vibrational motion of A and B about their respective equilibrium positions, \vec{R}_0^A and \vec{R}_0^B . However, any mechanism that induces a dynamic sign change in J [44, 71, 72] will enable the design of desired entanglement trajectories, such as those shown in Fig. 1(d). We note that an alternating exchange sign can equivalently be achieved by applying a harmonic potential to the environmental qudit C , rather than to A or B .

The operating regime considered here is governed by the competition between two mechanisms: the Kondo effect, which screens a local moment into a many-body singlet [75], and the RKKY interaction, which produces an oscillatory ordering of local moments [41, 45, 49, 76]. In this paper, we concentrate on the RKKY-dominated regime, characterized on the Doniach phase diagram by a sufficiently small exchange coupling J_{sd} —or, equivalently, a low density of states at the Fermi level, $N(E_F)$. This condition ensures that the RKKY interaction scale, $J \sim J_{sd}^2 N(E_F)$, exceeds the Kondo energy scale $k_B T_K$, where $T_K \sim \exp[-1/(N(E_F) J_{sd})]$ [77, 78].

We focus on the motion-driven scheme, where capital R denotes the locations of the exchange nodes (zeros of J). Specifically, we set the equilibrium positions

$\vec{R}_0^A = \vec{R}_n$ and $\vec{R}_0^B = \vec{R}_{-n}$ such that the A and B qubits vibrate about the n -th and $(-n)$ -th nodes, respectively, satisfying $J(\vec{R}_0^{A/B}) = 0$. According to Eq. (4), the spatial evolution of the qubits, characterized by the vibrational motion parallel to the 2DEG plane, is given by

$$r^{A/B}(t) = R_0^{A/B} + \mathcal{R}^{A/B} \cos(\omega^{A/B} t + \phi^{A/B}), \quad (5)$$

with frequency $\omega^{A/B}$, phase constant $\phi^{A/B}$, and displacement amplitude $\mathcal{R}^{A/B}$. We assume small amplitudes $\mathcal{R}^{A/B} \ll |\vec{R}_{n+1} - \vec{R}_n|$ so that the exchange interaction in Eq. (3) can be linearized with respect to the distance $r^{A/B}$ as

$$\begin{aligned} J(r^{A/B}(t)) \approx & J\left(R_0^{A/B}\right) + \\ & \left. \frac{dJ(r^{A/B})}{dr^{A/B}} \right|_{r^{A/B}=\vec{R}_0^{A/B}} \times \\ & \left(r^{A/B} - R_0^{A/B} \right). \end{aligned} \quad (6)$$

Substituting Eq. (5) into this expansion yields

$$J^{A/B}(t) = J_0^{A/B} \cos(\omega^{A/B} t + \phi^{A/B}), \quad (7)$$

with the alternating-exchange amplitude defined as

$$J_0^{A/B} = \frac{dJ(r^{A/B})}{dr^{A/B}} \bigg|_{r^{A/B}=\vec{R}_0^{A/B}} \mathcal{R}^{A/B}. \quad (8)$$

Consequently, the A - B system in Eq. (3) effectively evolves under the time-dependent Hamiltonian,

$$H(t) = J^A(t) \vec{\sigma}^A \cdot \vec{S}^C + J^B(t) \vec{\sigma}^B \cdot \vec{S}^C \quad (9)$$

$$= J_0^A \cos(\omega^A t + \phi^A) \vec{\sigma}^A \cdot \vec{S}^C \\ + J_0^B \cos(\omega^B t + \phi^B) \vec{\sigma}^B \cdot \vec{S}^C. \quad (10)$$

We elucidate the role of the dynamical exchange $J(t)$ when the two qubits vibrate at the same frequency $\omega^A = \omega^B = \omega$, specifically for the synchronous regimes of in-phase ($\Delta\phi \equiv \phi^A - \phi^B = 0$) and antiphase ($\Delta\phi = \pm\pi$) motion. The system dynamics are governed by the Liouville-von Neumann equation,

$$\frac{d\varrho(t)}{dt} = -i[H(t), \varrho(t)], \quad (11)$$

where $\hbar \equiv 1$. The formal solution is

$$\varrho(t) = U(t) \varrho_0 U^\dagger(t), \quad (12)$$

with the evolution operator

$$U(t) = \tau \left\{ \exp \left[-i \int_0^t H(t') dt' \right] \right\}, \quad (13)$$

and the initial density matrix (DM) $\varrho(t=0) \equiv \varrho_0$. Crucially, in these synchronous regimes, the time dependence in Eq. (10) becomes a common scalar factor, allowing the Hamiltonian to be factorized into a time-dependent amplitude and a time-independent operator. Consequently, the Hamiltonian commutes with itself at different times ($[H(t), H(t')] = 0$), allowing the time-ordering operator τ to be dropped.

Consider the in-phase case where $\phi_A = \phi_B \equiv \phi$. Direct integration yields

$$U(t) = \exp[-iI(t)] \times \sum_{k=x,y,z} (\sigma_k^A \eta_{J,k}^A + \sigma_k^B \eta_{J,k}^B) S_k^C \quad (14)$$

where the time-dependence is fully captured by the quantity

$$I(t) = \frac{J_0}{\omega} [\sin(\omega t + \phi) - \sin(\phi)]. \quad (15)$$

We refer to $I(t)$ as the ETI, which quantifies the accumulated exchange interaction [34]. Here, we have generalized to anisotropic exchange by defining the vector amplitudes

$$\vec{J}_0^{A/B} = (J_{0,x}^{A/B}, J_{0,y}^{A/B}, J_{0,z}^{A/B}) = J_0 \vec{\eta}_J^{A/B}. \quad (16)$$

We set the scaling such that $J_0 \equiv |\vec{J}_0^A|$ and $\vec{\eta}_J^{A/B}$ is a unit vector. The coupling ratio is defined as $\gamma \equiv J_0^A/J_0^B$, implying the relative vector components are related by

$$\eta_{J,k}^B = \frac{\eta_{J,k}^A}{\gamma}, \quad (17)$$

with $k \in \{x, y, z\}$. For antiphase motion, the condition $\phi^A = \phi^B \pm \pi$ yields a negative coupling ratio ($\gamma < 0$), as $\cos(\phi + \pi) = -\cos(\phi)$. Employing the eigen-decomposition of the time-independent operator,

$$\sum_{k=x,y,z} (\sigma_k^A \eta_{J,k}^A + \sigma_k^B \eta_{J,k}^B) S_k^C = V D V^\dagger, \quad (18)$$

the DM evolution reduces to

$$\begin{aligned} \varrho(t) = & V \exp[-iI(t)D] V^\dagger \\ & \times \varrho_0 \\ & \times V \exp[iI(t)D] V^\dagger, \end{aligned} \quad (19)$$

with $V(D)$ the eigenvector (diagonal-eigenvalue) matrix. This result highlights that the exchange strength J_0 and time t influence the system solely through the single parameter $I(t)$. Time reversal is thus effected by reversing the sign of the exchange profile to retrace $I(t)$. The validity of this scalar ETI extends beyond the linearized harmonic motion shown above. Generally, as long as the ratio between the couplings remains constant in time—i.e., $\vec{J}^A(t) = \gamma \vec{J}^B(t)$ —the Hamiltonian factorizes into a common time-dependent scalar factor and a static spin operator. In such cases, the ETI takes the general form, up to a constant,

$$I(t) = \int_0^t J^{A/B}(t') dt'. \quad (20)$$

This factorization allows the complex dynamics to be mapped onto the single ETI, enabling the designable trajectories discussed below. Conversely, the out-of-phase case requires extending the ETI to a vector form, yielding irregular trajectories where reversing the exchange profile sign does not effect time reversal. This regime is detailed in Section III B. Physically, the calculations above assume the fast-motion limit, implying the qubit vibration frequency is sufficiently high that the spatial RKKY profile (determined by the electron spin polarization in the 2DEG) does not fundamentally reconfigure within one period. We further note that the constant exchange ratio γ required for this Hamiltonian factorization can be engineered via coherent control of external fields, such as the dynamical gate voltage $V_G(t)$ [see Fig. 1(b)] or applied electromagnetic waves.

To quantify the deviation of a state from the A - B entanglement-separability boundary, we compute the reduced DM

$$\begin{aligned} \rho(t) \equiv & \rho^{AB}(t) \\ = & \text{Tr}_C[\varrho(t)], \end{aligned} \quad (21)$$

TABLE I. Bell-state weightings (W_1 – W_{14}) and characteristic times T^* (\hbar/J_0) for mixed and pure states with $\Delta\phi = 0$. Depending on the initial weighting, the dynamics near $t \approx 0$ exhibit entanglement sudden death (ESD), sudden birth (ESB), or transition of zero duration (TZD). The *penetrable* entanglement switch parameter ε sets whether the system begins in the entangled regime ($\varepsilon > 0$, as in ESD), separable regime ($\varepsilon < 0$, as in ESB), or on the boundary ($\varepsilon = 0$).

Weighting ($w_{\alpha+}, w_{\alpha-}, w_{\beta+}, w_{\beta-}$)	T^* (\hbar/J_0) for Mixed States	Dynamics of Mixed States Near $t \approx 0$	T^* (\hbar/J_0) for Pure States	Dynamics of Pure States Near $t \approx 0$
$W_1 = \left(\frac{1+\varepsilon}{2}, \frac{1-\varepsilon}{2}, 0, 0\right)$	0.6285	ESD	N/A	TZD
$W_2 = \left(\frac{1-\varepsilon}{2}, 0, \frac{1-\varepsilon}{2}, 0\right)$	2.6185	ESD	N/A	TZD
$W_3 = \left(\frac{1+\varepsilon}{2}, 0, 0, \frac{1-\varepsilon}{2}\right)$	0.6283	ESD	N/A	TZD
$W_4 = \left(0, \frac{1+\varepsilon}{2}, \frac{1-\varepsilon}{2}, 0\right)$	2.6185	ESD	N/A	TZD
$W_5 = \left(0, \frac{1+\varepsilon}{2}, 0, \frac{1-\varepsilon}{2}\right)$	0.6283	ESD	N/A	TZD
$W_6 = \left(0, 0, \frac{1+\varepsilon}{2}, \frac{1-\varepsilon}{2}\right)$	N/A	TZD	N/A	TZD
$W_7 = \left(\frac{1+\varepsilon}{2}, \frac{1-\varepsilon}{4}, \frac{1-\varepsilon}{4}, 0\right)$	0.8801	ESD	0.5525	ESB
$W_8 = \left(0, \frac{1+\varepsilon}{4}, \frac{1-\varepsilon}{4}, \frac{1-\varepsilon}{4}\right)$	0.8779	ESD	0.2822	ESB
$W_9 = \left(\frac{1-\varepsilon}{4}, 0, \frac{1+\varepsilon}{4}, \frac{1-\varepsilon}{4}\right)$	0.5139	ESD	0.3124	ESD
$W_{10} = \left(\frac{1-\varepsilon}{4}, \frac{1-\varepsilon}{4}, 0, \frac{1+\varepsilon}{2}\right)$	2.8819	ESB	0.4422	ESB
$W_{11} = \left(\frac{1+\varepsilon}{2}, \frac{1-\varepsilon}{6}, \frac{1-\varepsilon}{6}, \frac{1-\varepsilon}{6}\right)$	0.7652	ESD	0.5929	ESB
$W_{12} = \left(\frac{1-\varepsilon}{6}, \frac{1-\varepsilon}{2}, \frac{1-\varepsilon}{6}, \frac{1-\varepsilon}{6}\right)$	0.7652	ESD	0.6036	ESD
$W_{13} = \left(\frac{1-\varepsilon}{6}, \frac{1-\varepsilon}{6}, \frac{1+\varepsilon}{2}, \frac{1-\varepsilon}{6}\right)$	0.5444	ESD	0.1996	ESD
$W_{14} = \left(\frac{1-\varepsilon}{6}, \frac{1-\varepsilon}{6}, \frac{1-\varepsilon}{6}, \frac{1+\varepsilon}{2}\right)$	2.2990	ESB	0.4406	ESB

obtained by tracing out the spin degrees of freedom of qubit C . We then employ the concurrence \mathcal{C}_E [79–81], *extended to admit negative values*,

$$\mathcal{C}_E(t) = 2\kappa_{\max} - K \quad (22)$$

where $\kappa \in \{\kappa_1, \kappa_2, \kappa_3, \kappa_4\}$ are the eigenvalues of the matrix

$$\sqrt{\sqrt{\rho(t)}\rho'(t)\sqrt{\rho(t)}}, \quad (23)$$

with $\kappa_{\max} = \max(\kappa)$, and $K = (\kappa_1 + \kappa_2 + \kappa_3 + \kappa_4)$. Here, $\rho'(t)$ is constructed from the complex conjugate $\rho(t)^*$ via the transformation,

$$\rho'(t) = \sigma_y^{\otimes 2} \rho(t)^* \sigma_y^{\otimes 2}. \quad (24)$$

Importantly, positive values of $\mathcal{C}_E(t)$ indicate entanglement, while negative values indicate separability. A larger absolute value $|\mathcal{C}_E(t)|$ signifies a greater deviation from the boundary. As verified by our numerical calculations, this metric $\mathcal{C}_E(t)$ aligns qualitatively with the entanglement negativity [58].

B. Boundary-proximal initial states

Although Eq. 19 allows for an explicit expression of the evolved $\mathcal{C}_E(t)$ and predictions on the existence of ESD and ESB (see Appendix A) in the mixed-state case, to systematically explore the navigation of entanglement trajectories in both mixed and pure states, we employ the ISs characterized by the entanglement switch parameter (ESP [58]) ε . The ESP is defined as penetrable if it allows the IS to be tuned across the entanglement-separability boundary: $\varepsilon > 0$ corresponds to entangled

states, while $\varepsilon < 0$ denotes separable states. By selecting ISs near $|\varepsilon| \approx 0$, we can investigate critical dynamics such as ESD and ESB, with the exact $\varepsilon = 0$ corresponding to the states at the boundary. The initial reduced DM, $\rho_0 \equiv \rho(t=0)$, is expanded in the basis of the four Bell states,

$$|\alpha^\pm\rangle = \sqrt{\frac{1}{2}} |\uparrow, \uparrow\rangle \pm \sqrt{\frac{1}{2}} |\downarrow, \downarrow\rangle \quad (25)$$

and

$$|\beta^\pm\rangle = \sqrt{\frac{1}{2}} |\uparrow, \downarrow\rangle \pm \sqrt{\frac{1}{2}} |\downarrow, \uparrow\rangle, \quad (26)$$

yielding the form

$$\rho_0 = w_{\alpha+} |\alpha^+\rangle \langle \alpha^+| + w_{\alpha-} |\alpha^-\rangle \langle \alpha^-| + w_{\beta+} |\beta^+\rangle \langle \beta^+| + w_{\beta-} |\beta^-\rangle \langle \beta^-, \quad (27)$$

where the weighting $W = (w_{\alpha+}, w_{\alpha-}, w_{\beta+}, w_{\beta-})$ is normalized, $w_{\alpha+} + w_{\alpha-} + w_{\beta+} + w_{\beta-} = 1$. The specific weightings considered are listed in the first column of Table I, where nonzero weights are set near 1/2. For mixed states ($\text{Tr}[(\rho_0)^2] < 1$), we initialize the system as $\rho_0 \otimes |\uparrow\rangle \langle \uparrow|$, with the central spin-1/2 C set to the spin-up state $|S^C\rangle = |\uparrow\rangle$. For pure states ($\text{Tr}[(\rho_0)^2] = 1$), we construct the IS as $\varrho_0 = |\psi_0\rangle \langle \psi_0|$, with

$$|\psi_0\rangle = \sum_{\substack{i=\alpha^+, \alpha^-, \beta^+, \beta^- \\ w_i \neq 0}} \sqrt{w_i} |i^C\rangle \otimes |i\rangle, \quad (28)$$

where the summation runs over the basis states $|i\rangle \in \{|\alpha^\pm\rangle, |\beta^\pm\rangle\}$ corresponding to the nonzero weights w_i in Table I. The environmental states $|i^C\rangle$ map to the spin- z eigenstates $|m\rangle$ of C arranged in descending order

$(|m = S^C\rangle, |S^C - 1\rangle, \dots, |-S^C\rangle)$. The spin S^C is chosen to match the number of nonzero Bell components in the expansion: $S^C = 1/2$ for W_{1-6} , $S^C = 1$ (qutrit) for W_{7-10} , and $S^C = 3/2$ (qudit, $d = 4$) for W_{11-14} . Generally, *ISs constructed from more than two Bell states (W_{7-14}) are penetrable*, i.e., facilitate boundary crossings (ESD/ESB) as ε changes sign, whereas ISs limited to two Bell states (W_{1-6}) typically exhibit ESD or TZD. For instance, all W_{1-6} *pure* states yield the TZD (see Table I). As the trivial dynamics of the TZD do not result in boundary crossings, these cases are not examined in the following results.

III. RESULTS

In the simulation results presented below, bold italic letters M and P in the figures denote the cases of mixed and pure states, respectively. Unless otherwise specified, the following defaults are adopted in the numerical simulations. Isotropic exchange is assumed within the configuration shown in Fig. III A(a) [Eq. (5)], with identical vibrational frequencies ($\omega^A = \omega^B \equiv \omega$) and exchange strengths ($J_0^A = J_0^B \equiv J_0$), yielding $\gamma = 1$. The qubit motion commences from a position outside the exchange nodes, with the phase at $\phi_B = 0$. For in-phase and antiphase motions (Sec. III A), the dynamics are governed by Eq. (19), while Eq. (13) describes the out-of-phase motion (Sec. III B). All analytical results have been verified to match the direct numerical integration of the master equation [Eq. (11)]. Energies are in units of $|J_0| \equiv 1$, and time t in units of $\hbar/|J_0|$. To observe critical boundary dynamics (ESD, ESB, or TZD), the ESP $|\varepsilon| = 0.01$ is selected, with $J_0 = -1$. The characteristic operating period T^* is determined from the time t^* required for the state to reach the entanglement-separability boundary

$$\mathcal{C}_E(t^*) = 0. \quad (29)$$

where the relation is given by

$$t^* = T^*/4, \quad (30)$$

The resulting values of T^* (and the corresponding frequency $f = 1/T^*$) for the selected ε are listed in Table I.

Note that the RKKY-driven spin dynamics can be disrupted by ferromagnetic resonance (FMR) in the few-GHz range, where resonant energy absorption enhances spin precession. To ensure that the RKKY exchange remains the dominant mechanism, operation away from this resonance regime is required. This can be achieved by reducing the vibrational amplitude or using a proximate 2D Fermi-sea substrate [Fig. 1(b)] yielding $|J_0| \lesssim 1 \mu\text{eV}$; this upper limit corresponds to a characteristic frequency $|J_0|/\hbar \approx 1.52 \times 10^9 \text{ rad/s}$ (or equivalently, 0.24 GHz), which is well separated from the FMR band. Furthermore, bearing in mind that sign changes in $J^{A/B}(t)$ signify time and trajectory reversal, we can tailor the entanglement profile as demonstrated below.

A. In-phase and antiphase vibrations

This section examines the entanglement trajectories for in-phase and antiphase vibrations. Because the underlying analysis is identical in both cases, as the exchange-time integral (ETI) applies equally, we restrict the discussion to the in-phase case. For mixed states, the characteristic period T^* , defined by $\mathcal{C}_E(T^*/4) = 0$, can be estimated analytically in the short-time regime as detailed in Appendix B. Substituting T^* into Eq. (15) yields the weight-dependent characteristic ETI,

$$I_W^* \equiv I(T^*/4). \quad (31)$$

Since the entanglement dynamics depend solely on the ETI, any exchange dynamics—whether or not it involves vibrations—described by the general expression (20) in Eq. (19), with the same initial weight W and an ETI satisfying I_W^* , will necessarily reach the entanglement-separability boundary at $t = T^*/4$. The trajectories can therefore be systematically engineered through frequency control. For vibrations with $T = T^*$, the ETI indicates a trajectory reversal at $t = T^*/4$. These trajectories correspond to reversible navigation, in which the qubit-state evolution is governed by the periodic accumulation and unwinding of the ETI, so that reversing the sign of $J(t)$ effectively retraces the entanglement history. Consequently, oscillatory trajectories arise for $T \gtrsim T^*$, $T = T^*$, and $T \lesssim T^*$, corresponding to snake, bouncing, and entangled- or separable-confined profiles, respectively. The snake trajectory (for slightly larger $T \gtrsim T^*$) periodically crosses the entanglement-separability boundary. The bouncing trajectory (for $T = T^*$) reverses immediately upon reaching the boundary, corresponding to a TZD. The entangled/separable trajectory (for slightly smaller $T \lesssim T^*$) remains confined to one subspace without crossing the boundary. These trajectories are shown in Fig. 2 for both mixed and pure states.

For entanglement trajectories based on non-periodic motion, we consider the same vibrational scenario, except that the qubit motion is abruptly halted upon reaching the exchange nodes. The exchange coupling follows Eqs. (5) and (7), now modulated by a unit-step function Θ ,

$$J^{A/B}(t) = J_0 \cos\left(\frac{2\pi t}{T^*}\right) \Theta\left(\frac{T^*}{4} - t\right). \quad (32)$$

Figure 3 shows the resulting trajectories for both mixed and pure states. After $t \geq T^*/4$, the qubits remain pinned at the entanglement-separability boundary, forming a boundary-residing trajectory. Notably, although the motion stops abruptly, the entanglement exhibits a smooth approach to zero $d\mathcal{C}_E(t)/dt|_{t=T^*/4} = 0$ in Fig. 3. As a result, neither ESD nor ESB occurs. This demonstrates that an abrupt halt of the qubit motion, even involving a kinetic discontinuity (abrupt change in velocity), does not necessarily induce sudden entanglement dynamics.

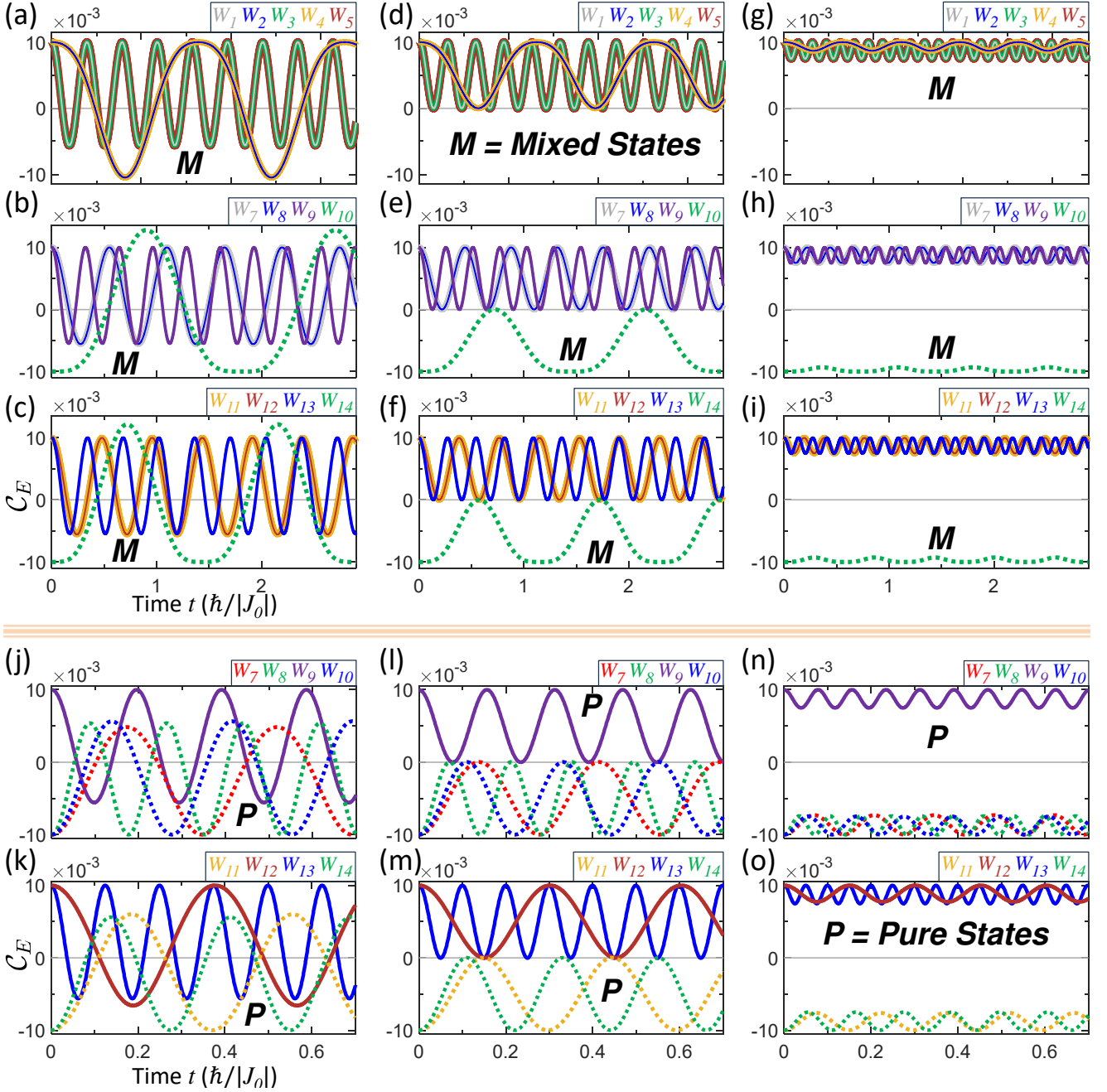


FIG. 2. Entanglement trajectories for mixed (marked by bold italic M) and pure (marked by bold italic P) states under in-phase vibrations. The extended concurrence $C_E(t)$ is plotted versus time t for various Bell-state weightings W_{1-14} (see corresponding color text labels). The upper panels (a)–(i) display the dynamics for mixed states: (a)–(c) show snake trajectories ($T = 1.25 T^*$), (d)–(f) show bouncing trajectories ($T = 1.25 T^*$), and (g)–(i) exhibit entangled/separable trajectories ($T = 1.25 T^*$). The lower panels (j)–(o) show the corresponding dynamics for pure states: snake trajectories in (j) and (k), bouncing trajectories in (l) and (m), and entangled/separable trajectories in (n) and (o). For the bouncing trajectories, solid lines denote initially entangled states ($\varepsilon > 0$), while dashed lines denote separable states ($\varepsilon < 0$).

Alternatively, the boundary-residing behavior is also accessible by employing a smooth (continuous-velocity) stop, where the exchange in Eq. (32) follows $\cos^2(\theta)$ instead of $\cos(\theta)$. In this case, T^* is recomputed according to Eqs. (30) and (29). Specifically, this protocol realizes

a pulse trajectory by employing the time dependence

$$J^{A/B}(t) = J_0 \cos^2\left(\frac{2\pi t}{T^*}\right) \Theta\left(\cos\left(\frac{2\pi t}{T^*}\right)\right) \times (-1)^{\text{floor}(4t/T^*)}, \quad (33)$$

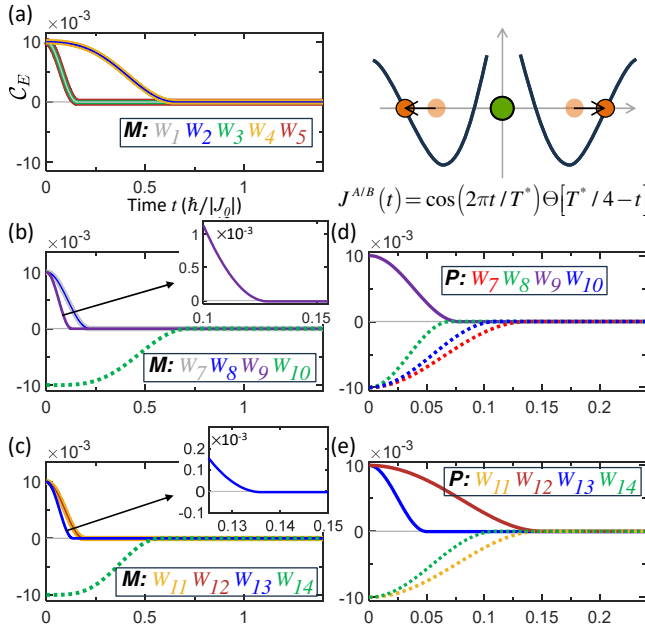


FIG. 3. Entanglement trajectories originating from abruptly halted vibrational motion (schematic in the upper right) for (a)–(c) mixed states and (d)–(e) pure states with different weightings. The qubits remain at the entanglement-separability boundary after $t \geq T^*/4$, producing a boundary-residing trajectory. The insets show zoomed views near the stopping time $t = T^*/4$. All trajectories approach the boundary tangentially (smoothly), despite the abrupt cessation of motion.

which corresponds to a temporary dwell of the motion whenever the qubit reaches an exchange node (see the schematics in Fig. 4). Here, the function *floor* denotes rounding toward negative infinity. Figure 4 shows the resulting pulse trajectories for both mixed and pure states obtained from Eq. (33). The dwell duration is $T^*/2$, spanning the intervals $(2p+1)T^*/4$ to $(2p+2)T^*/4$ with $p = 0, 1, 2, \dots$. This sequence produces repeated boundary-residing segments, generating entangled (solid lines) and separable (dashed lines) pulse trains. A single pulse can be produced by imposing a permanent stop. We note, however, that, for boundary-residing and pulsed trajectories, quantum position fluctuations δr prevent the qubit position from being perfectly fixed at the exchange node. These fluctuations can be mitigated using position-squeezed states [82–85], ensuring that δr remains much smaller than the vibration amplitude. In practice, for entangled (separable) pulses, a slightly larger value of T^* is chosen so that the fluctuation in the extended concurrence δC_e remains well below (above) the boundary. Due to the uncertainty principle, the boundary-residing trajectory is fundamentally approximate in the motion-driven scheme, leading to residual fluctuations around the boundary.

When qubits are initialized closer to the exchange nodes, a finite vibrational phase $\phi \neq 0$ can be intro-

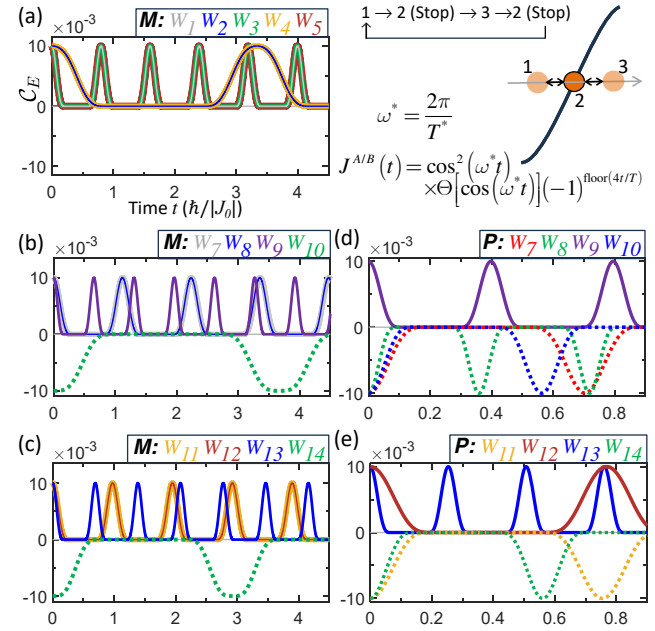


FIG. 4. Entanglement pulses generated by controlled stopping and restarting of qubit cyclic motion, as shown schematically in the upper-right panel. The qubits halt temporarily at the exchange nodes, producing entangled (solid) and separable (dashed) pulses. Panels (a)–(c) show mixed states, while panels (d) and (e) show pure states. The trajectories include repeated boundary-residing segments, with the qubits departing from and returning to the boundary between these segments, thereby forming pulse trains.

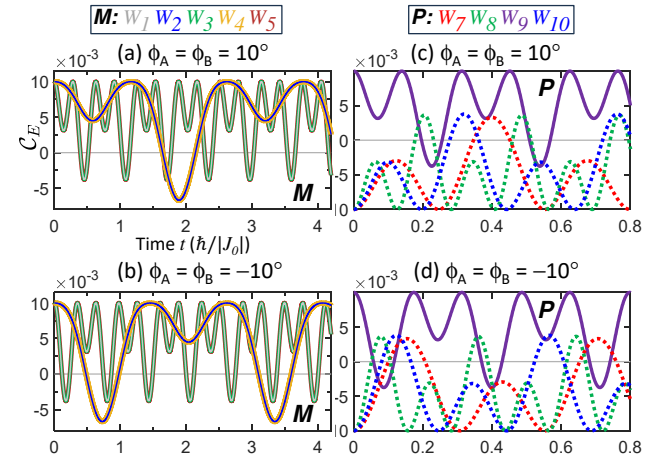


FIG. 5. Entanglement trajectories for qubits initialized with a finite vibrational phase $\phi \neq 0$. Qubits vibrating toward ($\phi = 10^\circ$) or away ($\phi = -10^\circ$) from the exchange nodes with period $T = T^*$ in Table I produce snake trajectories. Panels (a) and (b) show mixed states with weightings W_{1-5} , and panels (c) and (d) show pure states with weightings W_{7-10} . A finite ϕ causes asymmetric vertical shifts, while reversing its sign introduces horizontal phase shifts. Solid and dashed lines represent positive ($\varepsilon > 0$) and negative ($\varepsilon < 0$) ESP, respectively.

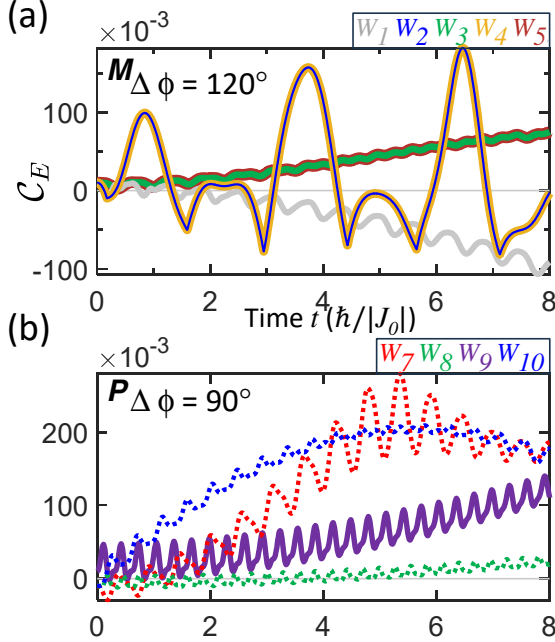


FIG. 6. Out-of-phase entanglement trajectories for (a) mixed states with $\Delta\phi = 120^\circ$ and (b) pure states with $\Delta\phi = 90^\circ$. Solid lines represent initially entangled states with positive ESP, while dashed lines represent initially separable states with negative ESP. Vibration periods $T = T^*$ from Table I are used. The curves illustrate how out-of-phase motion drives the entanglement trajectories away from the boundary (horizontal gray lines).

duced. This modification preserves the tunability of the trajectories via the period but introduces asymmetry in the entanglement evolution. As shown in Fig. 5, using $T = T^*$ from Table I, similar snake trajectories emerge for selected weightings: W_{1-5} for mixed states and W_{7-10} for pure states. To understand the origin of the snake profile, we compare it to the standard ($\phi = 0$) bouncing trajectories. While the vibrational amplitude is identical, the finite phase implies that the qubits are initialized closer to the exchange node. Consider an entangled IS with $\phi > 0$. After $t = 0$, the interval before the qubits reach the node is shortened, leading to a reduced accumulation of the ETI and a correspondingly weaker loss of entanglement. This initial phase therefore produces a shallow reversal entirely within the entangled subspace. Subsequently, after passing through the node, the qubits traverse the full range of motion until returning to the node. The ETI accumulated during this interval matches the standard bouncing case and exceeds the initial minor reduction. Consequently, this second swing drives the trajectory across the boundary into the separable subspace, giving rise to the characteristic snake profile. By the same reasoning, this snake trajectory is also realized for separable ISs.

In other words, a finite ϕ induces asymmetric vertical shifts, reflecting the difference in the ETI accumulation between consecutive entanglement recoveries. By con-

trast, reversing the sign of ϕ means the qubits initially move in the opposite direction; this effectively introduces a horizontal phase shift, as observed by comparing panels (a) with (b) and (c) with (d) in Fig. 5. The same argument applies to all other weightings exhibiting ESD and ESB listed in Table I. For brevity, only the representative cases (mixed states with W_{1-5} and pure states with W_{7-10}) are shown in the subsequent figures.

Importantly, for both in-phase and antiphase motion, we emphasize that the proposed device—characterized by alternating exchange signs—possesses built-in error correction against dephasing for oscillatory trajectories, Figs. 2, 4, and 5. Phase coherence is preserved because the rapid phase accumulation during the ferromagnetic ($J < 0$) intervals is compensated by the rapid phase unwinding during the antiferromagnetic ($J > 0$) intervals, refocusing the state and producing an echo-like correction [32, 74]. Notably, being exchange-free, the node serves as an ideal location for qubits to idle. Conversely, prior to applying the confinement potential that yields the vibrations, the stable ground state resides at either the local maximum or minimum of J , making these points natural sites for entanglement initialization and development. While in-phase motion provides a robust baseline for tailoring entanglement dynamics, the strict periodicity of the evolution limits the accessible state space, particularly at short operation times. To overcome this limitation and access larger entanglement values, we now turn to the out-of-phase configuration, where the vibrational phases are shifted relative to one another.

B. Out-of-phase vibrations

The introduction of a relative vibrational phase difference $\Delta\phi = \phi^A - \phi^B \neq 0$ defines the regime of out-of-phase vibrations. In this regime, the time-evolution operator can no longer be parameterized by a single ETI $I(t)$, as was done in Eq. (14). Instead, the dynamics are governed by two distinct integrals, $I^A(t)$ and $I^B(t)$. Although these integrals share the same functional form, their relative phase mismatch prevents the DM in Eq. (19) from retaining the strict periodic structure associated with a unified $I(t)$. Consequently, the resulting entanglement evolution becomes generally non-periodic.

Indeed, as shown in Fig. 6, the concurrence ceases to follow the simple repeating patterns observed in the in-phase or antiphase cases. Panels (a) and (b) illustrate the evolution for mixed and pure states, with phase differences of $\Delta\phi = 120^\circ$ and $\Delta\phi = 90^\circ$, respectively. The trajectories tend to drift progressively farther from the entanglement-separability boundary, exhibiting a slow overall growth upon which fast modulations (sub-oscillations) are superimposed. Notably, weightings W_3 and W_5 (mixed states) and W_{7-10} (pure states) achieve significantly higher entanglement values than their $\Delta\phi = 0$ counterparts. Furthermore, W_2 and

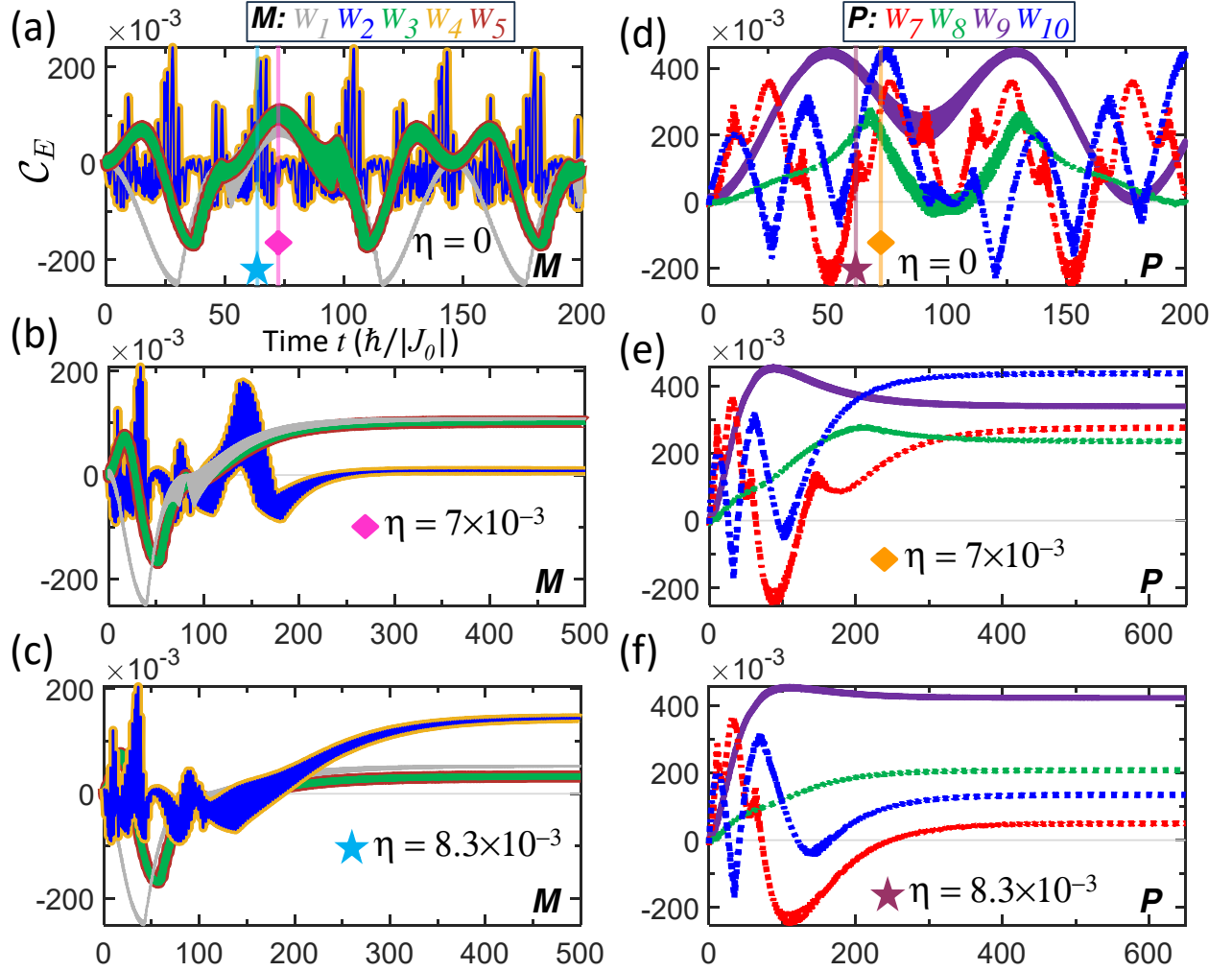


FIG. 7. Entanglement evolution for (a)–(c) mixed states and (d)–(f) pure states with out-of-phase vibrations at $\Delta\phi = 30^\circ$. The vibration period $T = T^*$ from Table I is used. The undamped cases ($\eta = 0$) are shown in (a) and (d). The damped cases are shown with damping strength $\eta = 7 \times 10^{-3}$ (in units of $|J_0|/\hbar$) in (b) and (e) (diamond markers), and $\eta = 8.3 \times 10^{-3}$ in (c) and (f) (star markers). The vertical lines in (a) and (d) indicate the corresponding stabilization time t_s observed in the damped regimes. The transient band-like curves arise from fast and closely spaced entanglement modulations. A weaker damping strength leads to a larger postponement of t_s . Under damping, time effectively slows down, causing the trajectories to appear stretched before t_s and ultimately resulting in a time-frozen trajectory. For example, W_7 in (d) shows a minimum around $t = 50$, while in (e) and (f) this minimum occurs later, around $t = 100$.

W_4 (mixed states) exhibit swings with growing amplitude that cross the boundary multiple times. This complex behavior arises from the interference between the distinct accumulation rates of $I^A(t)$ and $I^B(t)$.

Figure 6 demonstrates that out-of-phase motion enables access to quantum states and high-entanglement subspaces that are inaccessible under strictly periodic motion ($\phi^A = \phi^B$). This regime highlights the potential of phase-engineered, alternating RKKY coupling to create highly versatile and non-repetitive entanglement trajectories. However, a key limitation in this scenario is that the trajectories do not naturally converge to a stable value, restricting their direct applicability for state preparation. To address this, we introduce damping mechanisms that provide a route to stabilize the trajec-

tories.

In the out-of-phase regime where $\phi^A \neq \phi^B$, the exchange integrals $I^A(t)$ and $I^B(t)$ are generally not proportional. However, the introduction of damping fundamentally alters this behavior. Unlike the previous cases, damping causes the vibrational amplitude to decay, driving each ETI to converge to a distinct fixed value, $I^{A/B}(t \rightarrow \infty)$, as the qubits eventually settle at the exchange node ($J = 0$). As a result, the system enters a frozen regime, stabilizing the generated entanglement. For the case of isotropic exchange modeled by $J^{A/B}(t) = J_0 \cos(\omega^{A/B}t + \phi^{A/B}) \exp(-\eta * t)$, the ETI can be expressed using Eq. (20) as

$$I^{A/B}(t) = \frac{-J_0}{\eta^2 + \omega^2} F^{A/B}(\omega, \eta, t) \exp(-\eta * t) + \frac{J_0}{\eta^2 + \omega^2} F^{A/B}(\omega, \eta, 0), \quad (34)$$

where the function $F^{A/B}(\omega, \eta, t)$ is defined as

$$\begin{aligned} F^{A/B}(\omega, \eta, t) &= \eta \cos(\omega t + \phi^{A/B}) \\ &\quad - \omega \sin(\omega t + \phi^{A/B}) \\ &= \sqrt{\eta^2 + \omega^2} \\ &\quad \times \cos\left[\omega t + \phi^{A/B} + \arctan\left(\frac{\omega}{\eta}\right)\right] \end{aligned} \quad (35)$$

Here, η represents the damping strength in units of $|J_0|/\hbar$. To streamline the analysis, we introduce the amplitude scaling factor,

$$\Gamma \equiv \frac{J_0}{\sqrt{\eta^2 + \omega^2}}, \quad (36)$$

and the shifted phase,

$$\Phi^{A/B} \equiv \phi^{A/B} + \arctan\left(\frac{\omega}{\eta}\right). \quad (37)$$

With these definitions, Eq. (34) simplifies to

$$\begin{aligned} I^{A/B}(t) &= -\Gamma \cos(\omega t + \Phi^{A/B}) \exp(-\eta * t) \\ &\quad + I^{A/B}(t \rightarrow \infty), \end{aligned} \quad (38)$$

where the ETI asymptotically approaches the constant stationary value,

$$I^{A/B}(\infty) = \Gamma \cos(\Phi^{A/B}). \quad (39)$$

Since the cosine function is bounded by unity (i.e., $-1 \leq \cos(\omega t + \Phi) \leq 1$), the ETI satisfies the inequality,

$$\begin{aligned} &\Gamma \cos(\Phi^{A/B}) - |\Gamma| \exp(-\eta * t) \\ &\leq I^{A/B}(t) \\ &\leq \Gamma \cos(\Phi^{A/B}) + |\Gamma| \exp(-\eta * t). \end{aligned} \quad (40)$$

This bound offers valuable physical insights. First, it shows that weaker damping (smaller η) and lower vibration frequencies (smaller ω) expand the accessible range of the ETI by increasing the magnitude of Γ . Accordingly, this expansion allows for greater achievable entanglement. Second, by comparing Eq. (40) with Eq. (39), we observe that $I^{A/B}(t)$ can transiently exceed its stationary value $I^{A/B}(\infty)$, particularly when η is small. Accordingly, the transient entanglement $\mathcal{C}_E(t)$ can surpass the final stabilized value $\mathcal{C}_E(\infty)$. Thus, by tuning ω and η , one can engineer the dynamics to target a specific, stable value of entanglement.

The features of this damped evolution are illustrated in Fig. 7 for a representative phase difference of $\Delta\phi = 30^\circ$, where panels (a)–(c) and (d)–(f) display results for mixed and pure states, respectively. Panels (a) and (d) present the undamped reference cases, while the subsequent panels introduce damping with $\eta = 7 \times 10^{-3}$ (diamond markers) and slightly stronger damping with $\eta = 8.3 \times 10^{-3}$ (star markers). Clearly, decreasing the damping strength delays the stabilization time t_s —the characteristic time scale beyond which the entanglement becomes effectively fixed. This delay is evident when comparing the damped panels (b) with (c) and (e) with (f), with the vertical lines in panels (a) and (d) marking the corresponding onset t_s of the frozen regime observed in the damped cases. In the early dynamics ($t < t_s$), the rapid entanglement modulations are so dense that they appear as continuous bands. During this phase, the trajectory profile retains the overall shape of the undamped case but with reduced amplitude and a slower effective evolution. However, the damping also causes the evolution to slow down, effectively stretching the profile along the time axis. For example, the first local minimum of W_3 in the undamped motion (a) occurs around $t = 30$, whereas in the damped motion (b) and (c), the corresponding first local minimum appears later, after $t = 45$. This delay reflects the slower accumulation of both $I^A(t)$ and $I^B(t)$, and thus the evolution, which eventually culminates in a time-frozen trajectory.

Accordingly, by optimizing the damping strength, one can maximize the final stable entanglement. As shown in Fig. 7, specific weightings— W_1, W_3, W_5 in (b); W_2, W_4 in (c); W_7, W_8, W_{10} in (e); and W_9 in (f)—yield frozen entanglement values that significantly exceed those achievable in the $\Delta\phi = 0$ case. We note that $I^{A/B}(t)$ in Eq. (38) reduces to Eq. (15) only in the limit $\eta = 0$ and $\Delta\phi = 0$. In the damped, out-of-phase scenario, $I^A(t)$ is no longer proportional to $I^B(t)$, marking a fundamental departure from the single-ETI eigen-decomposition used in Eq. (19). Physically, this damping model is also realizable in a scenario where the two qubits, A and B , move in opposite directions away from the central qudit C , thereby experiencing a spatially decaying, alternating RKKY interaction. *Up to here...*

IV. CONCLUSIONS

In conclusion, to navigate qubit entanglement trajectories, we propose an RKKY-based platform, Fig. 1, in which two spin qubits, A and B , couple to a central spin qudit C that induces an oscillatory spin polarization in the surrounding conduction electrons. To quantify the deviation from the entanglement-separability boundary, the concurrence is extended to include negative values; this extension enables a unified description of boundary-crossing dynamics. For qubits experiencing alternating exchange J around the node, the linearization (6) captures the relevant dynamics, yielding an effective time-

dependent Hamiltonian (9). The qubit spatial motion is mapped onto the ETI through the time dependence of the exchange interaction. The ETI (20), obtained by integrating the time-dependent exchange, acts as a single experimentally accessible control variable that parameterizes the state evolution via (19). With our interest placed on the spin-qubit entanglement rather than on the environmental qudit and conduction electrons, the orbital or spatial degrees of freedom are traced out, preserving the form of the ETI-ruled evolution for any spin-independent H_o .

We identify two complementary dynamical regimes, cyclic and non-cyclic navigation. First, cyclic navigation corresponds to periodic motion, enabling the recurrent restoration of the state. Specifically, for in-phase and anti-phase vibrations under a harmonic confinement potential, the ETI reduces to (15). Using weighted Bell-state DMs, Eq. (27), we demonstrate frequency-controlled transitions between snake, bouncing, and boundary-residing trajectories for both mixed states and pure states (Figs. 2 and 3). The FMR can be avoided by selecting realistic exchange values that yield the operating frequencies listed in Table I; the corresponding ETI values are computed accordingly (see Table II in Appendix A). By allowing temporary dwells at the nodes, entanglement pulse trains can be generated, with pulse separation controlled by the dwell duration, as shown in Fig. 4. A nonzero equal vibrational phase, $\phi = \phi^A = \phi^B$, induces an asymmetric vertical shift, while reversing its sign, $\phi \rightarrow -\phi$, produces a horizontal displacement of the trajectory (Fig. 5).

Second, non-cyclic navigation arises from out-of-phase exchange modulation. In this regime, the entanglement trajectory becomes non-periodic and is driven away from the boundary (6), enabling access to higher entanglement values but without essential stabilization. We employ damping to stabilize the dynamics: the exchange-time integral gradually converges, slowing the evolution and ultimately freezing the system at a fixed entanglement value, as illustrated in Fig. 7. This final fixed entanglement is tunable through the damping strength, phase difference, and vibrational frequencies, as indicated by the converged ETI given in Eq. (39). Together, cyclic and damped non-cyclic regimes provide complementary control strategies for reversible manipulation and robust state preparation, respectively.

In addition, the advantages of the proposed device are as follows. The system is scalable for pairwise entanglement between qubits A_q and A_{q+1} . For scalability, one simply relabels $A \rightarrow A_1$, $B \rightarrow A_2$, and $C \rightarrow C_1$ and then repeats the structure to form a chain $A_1-C_1-A_2-C_2-A_3 \cdots -A_{Q-1}-C_{Q-1}-A_Q$ consisting of Q qubits. The eigenvalue decomposition (18) then becomes

$$\sum_{q=1}^Q \sum_{k=x,y,z} \left(\sigma_k^{A_q} \eta_{J,k}^{A_q} \right) S_k^{C_q} = V D V^\dagger,$$

with $\eta_{J,k}^{A_1} = \gamma_2 \eta_{J,k}^{A_2} = \cdots = \gamma_n \eta_{J,k}^{A_n}$, and the same line

of argument based on the ETI (20) remains applicable. Moreover, partial correction of errors due to dephasing is integrated into the oscillatory trajectories. The nodes ($J = 0$) provide ideal locations for qubit information storage, while the shapeable trajectories enable the design of quantum encryption protocols and gate operations based on finite or repeated entanglement survival within specific time windows, achieving on-demand entanglement. In quantum sensing and metrology, the boundary-residing trajectory can be used for highly precise measurements of external observables that perturb the qubit toward or away from the entangled regime. The out-of-phase damping permits the establishment and maintenance of strong entanglement. Accordingly, the presented approach supports practical quantum devices that are both efficient, by shortening entanglement generation time, and stable, through the use of the exchange node, thereby advancing computation, secure communication, and sensing with entanglement as a tunable resource.

ACKNOWLEDGMENTS

One of the authors (S.-H. Chen) thanks Chang Yen Jui and Tsung-Wei Huang for valuable discussions. S-G Tan acknowledges support from the National Science and Technology Council (NSTC) of Taiwan under Grant No. NSTC 114-2112-M-034-001. C-R Chang acknowledges support from the NSTC under Grant No. NSTC 114-2112-M-033-005.

Appendix A: Extended concurrence in terms of ETI for mixed states and existence of snake trajectory

In contrast to pure states, for mixed states of the form (27), the evolution of the reduced DM $\rho(t)$ remains block diagonal. In this appendix, we demonstrate that such a structure allows the extended concurrence $\mathcal{C}_E(t)$ to be explicitly expressed as a functional of the ETI $I(t)$, providing a direct and compact method to track the entanglement evolution. In particular, we show that snake trajectories can be identified analytically without invoking the ESP ε .

Consider the spin-up IS with $S^C = \hbar/2$ and the qubits are described by (27). We set $\gamma = 1$ for isotropic exchange. Using (19) and (21) and defining the weight sums and differences as $w_s = w_{\alpha^+} + w_{\alpha^-}$ and $w_d = |w_{\alpha^+} - w_{\alpha^-}| > 0$, we introduce the functional dependence on the ETI via

$$C(I) = \cos(3I), \quad (\text{A1})$$

and

$$k(I) = 1 - C(I) \in [0, 2], \quad (\text{A2})$$

the reduced DM $\rho(t)$ then takes the form

$$\begin{pmatrix} \frac{9w_s + 8w_{\beta^+}k}{18} & 0 & 0 & \frac{w_d}{6}(1 + 2e^{-3iI}) \\ 0 & \frac{X^+}{18} & \frac{X^-}{18} & 0 \\ 0 & \frac{X^-}{18} & \frac{X^+}{18} & 0 \\ \frac{w_d}{6}(1 + 2e^{3iI}) & 0 & 0 & \frac{w_s(9 - 4k)}{18} \end{pmatrix}, \quad (\text{A3})$$

where $X^\pm = X \pm 9w_{\beta^-}$ and

$$X = 9w_{\beta^+} + 2k(w_s - 2w_{\beta^+}). \quad (\text{A4})$$

Recall that $\mathcal{C}_E(t)$ is constructed from the eigenvalues of (23), i.e., the square root of the eigenvalues ($\sqrt{\kappa_i} = \kappa_i$, $i \in \{1, 2, 3, 4\}$) of

$$\sqrt{\rho(t)}\rho'(t)\sqrt{\rho(t)}. \quad (\text{A5})$$

Since $\rho(t)$ and $\rho'(t)$ are positive semi-definite Hermitian matrices, Eq. (A5) and

$$R(t) = \rho(t)\rho'(t) \quad (\text{A6})$$

share the same eigenvalues $\tilde{\kappa}_i$. Substituting (A3) into this expression, we obtain $R(t)$ as

$$\begin{pmatrix} \frac{9 - 4k}{162} \left(\frac{9}{2}(w_s^2 + w_d^2) + 4w_s w_{\beta^+} k \right) & 0 & 0 & \frac{w_d}{54}(1 + 2e^{-3iI})(9w_s + 8w_{\beta^+}k) \\ 0 & \frac{X^2 + 81w_{\beta^-}^2}{162} & \frac{X^2 - 81w_{\beta^-}^2}{162} & 0 \\ 0 & \frac{X^2 - 81w_{\beta^-}^2}{162} & \frac{X^2 + 81w_{\beta^-}^2}{162} & 0 \\ \frac{w_s w_d}{54}(1 + 2e^{3iI})(9 - 4k) & 0 & 0 & \frac{9 - 4k}{162} \left(\frac{9}{2}(w_s^2 + w_d^2) + 4w_s w_{\beta^+} k \right) \end{pmatrix}. \quad (\text{A7})$$

Solving for the square roots of the eigenvalues of $R(t)$ yields

$$\kappa_1(k) = \frac{9w_{\beta^+} + 2(w_s - 2w_{\beta^+})k}{9} \quad (\text{A8})$$

$$\kappa_2(k) = \frac{\sqrt{9 - 4k}}{18} \left(\sqrt{w_s(9w_s + 8w_{\beta^+}k)} - 3w_d \right) \quad (\text{A9})$$

$$\kappa_3(k) = \frac{\sqrt{9 - 4k}}{18} \left(\sqrt{w_s(9w_s + 8w_{\beta^+}k)} + 3w_d \right) \quad (\text{A10})$$

and

$$\kappa_4 = w_{\beta^-}. \quad (\text{A11})$$

Note that $\kappa_3(k) > \kappa_2(k)$ as seen from the sign of the last term; thus, the maximum eigenvalue must be $\kappa_{\max} \in \{\kappa_1, \kappa_3, \kappa_4\}$.

As k increases, the condition

$$w_s > 2w_{\beta^+} \quad (\text{A12})$$

ensures that $\kappa_1(k)$ is an increasing function of k . Conversely, $\kappa_3(k)$ decreases with k because the decay of the prefactor $\sqrt{9 - 4k}$ dominates the growth of $\sqrt{w_s(9w_s + 8w_{\beta^+}k)}$. The equality $\kappa_1(k) = \kappa_3(k)$ always occurs within the interval $k \in [0, 2]$. This can be verified by analyzing the boundary values:

$$\kappa_1(0) = w_{\beta^+} \quad (\text{A13})$$

$$\kappa_3(0) = \frac{w_s + w_d}{2} \quad (\text{A14})$$

$$\kappa_1(2) = \frac{4w_s + w_{\beta^+}}{9} \quad (\text{A15})$$

$$\kappa_3(2) = \frac{\sqrt{w_s(9w_s + 16w_{\beta^+})} + 3w_d}{18}. \quad (\text{A16})$$

Under the condition in Eq. (A12), these boundaries imply $\kappa_1(0) - \kappa_3(0) < 0$ and $\kappa_1(2) - \kappa_3(2) > 0$. For simplicity, if we assume

$$w_{\beta^-} = 0, \quad (\text{A17})$$

then $\kappa_4 = 0$ and thus $\kappa_{\max} \in \{\kappa_1, \kappa_3\}$. Under this assumption, at the crossing point where $\kappa_1 = \kappa_3$, Eq. (22) guarantees that $\mathcal{C}_E = -\kappa_2 < 0$. Consequently, the question of whether a snake trajectory exists reduces to determining if a positive $\mathcal{C}_E > 0$ exists elsewhere within $k \in [0, 2]$. In fact, under the two conditions (A12) and (A17), we always find a positive value for \mathcal{C}_E at $k = 2$, $\mathcal{C}_E|_{k=2} = \kappa_1(2) - \kappa_2(2) - \kappa_3(2) > 0$, since $\kappa_1(2) > \kappa_2(2) + \kappa_3(2) = \sqrt{w_s(9w_s + 16w_{\beta^+})}/9$. Therefore, these two conditions—while not optimized for maximizing the balance between the entangled and separable residence times—are sufficient to produce a sign change in \mathcal{C}_E , signifying the emergence of the snake trajectory.

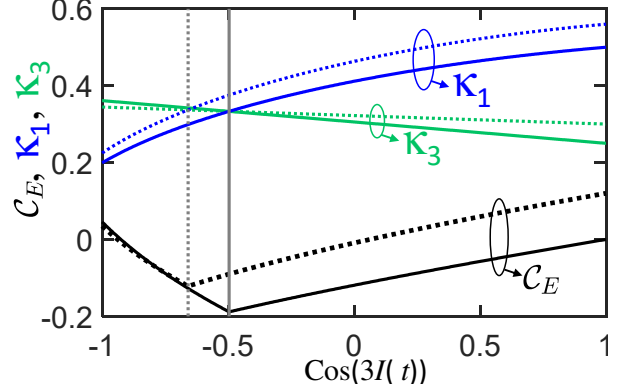


FIG. 8. Eigenvalues κ_1 (blue) and κ_3 (green), and extended concurrence $\mathcal{C}_E(t)$ (black) plotted as functions of $\cos(3I(t))$. The solid lines correspond to the weighting $(w_{\alpha^+}, w_{\alpha^-}, w_{\beta^+}, w_{\beta^-}) = (0.5, 0.25, 0.25, 0)$, while the dotted lines use $(w_{\alpha^+}, w_{\alpha^-}, w_{\beta^+}, w_{\beta^-}) = (0.56, 0.14, 0.3, 0)$. Both weightings satisfy the conditions in Eqs. (A12) and (A17), which produce the snake trajectory. The vertical lines mark the points where κ_1 and κ_3 cross.

The above analysis is illustrated in Fig. 8, which plots κ_1 , κ_3 , and \mathcal{C}_E as functions of $\cos(3I(t))$. Under the conditions (A12) and (A17), a crossing of the eigenvalues κ_1 and κ_3 results in negative concurrence $\mathcal{C}_E < 0$, whereas positive concurrence $\mathcal{C}_E > 0$ is recovered at $\cos(3I(t)) = -1$ (corresponding to $k = 2$), thereby realizing the snake trajectory. By controlling the time spent in the positive and negative \mathcal{C}_E regions via qubit motion, a programmable entanglement trajectory can be achieved.

Appendix B: Analytic estimation and numerical validation of the characteristic period

For mixed states, the characteristic period T^* , defined by the separability-boundary criterion $\mathcal{C}_E(T^*/4) = 0$, can be estimated analytically under the short-time approximation. Based on the results in Table 2 of Physica Scripta 100, 065114 (2025), which assumes a constant exchange interaction $J^{A/B}(t) = J^{A/B}$, we compute the analytic expressions for T^* valid up to order $O(dt^2)$. These approximate values are listed in Table II. To validate this approximation for our alternating-RKKY-exchange scheme, we compare the ETI calculated using these constant-exchange analytic periods against the full numerical results for sinusoidal exchange (as adopted in the main text). As shown in the last two columns of Table II, the constant-exchange ETI is in good agreement with the exact numerical values, confirming that the short-time analytic model provides a reliable estimate for the near-boundary dynamics studied herein.

TABLE II. Approximate analytic characteristic period T^* as a function of the entanglement switch parameter ε for *mixed* states, obtained with *time-independent* (constant) $J_x^{A/B}(t) = J_y^{A/B}(t) = J_z^{A/B}(t) = J_0$. Equivalent weightings that yield the same analytic form of T^* are grouped together. The expressions are valid up to order $O(dt^2)$, with dt the elapsed time after $t = 0$. The last two columns show the ETI for constant J^{AB} compared with the ETI for sinusoidal exchange in Table I, calculated without the short-time approximation.

Weightings	Approximate T^* (\hbar/J_0)	Constant J , Approximate $I\left(\frac{T^*}{4}\right)$	Sinusoidal J , $I\left(\frac{T^*}{4}\right)$ (Table I)
W_1, W_3, W_5	$\sqrt{\frac{16\varepsilon}{1+\varepsilon}}$	0.157	0.100
W_2, W_4	$2\sqrt{2}$	0.655	0.417
W_7, W_8	$\sqrt{\frac{32\varepsilon}{1+3\varepsilon}}$	0.220	0.140
W_9	$\sqrt{\frac{32\varepsilon}{3+5\varepsilon}}$	0.129	0.082
W_{10}	$\left[-\frac{1024\varepsilon(1+\varepsilon)}{(1-\varepsilon)^2}\right]^{1/4}$	0.721	0.459
W_{11}, W_{12}	$\sqrt{\frac{24\varepsilon}{(1+2\varepsilon)}}$	0.191	0.122
W_{13}	$\sqrt{\frac{12\varepsilon}{(1+2\varepsilon)}}$	0.136	0.087
W_{14}	$\left[-\frac{(384+768\varepsilon)\varepsilon}{(1-\varepsilon)^2}\right]^{1/4}$	0.575	0.366

<https://link.aps.org/doi/10.1103/PhysRevA.65.012101>.

[2] Horodecki, R., Horodecki, P., Horodecki, M. & Horodecki, K. Quantum entanglement. *Rev. Mod. Phys.* **81**, 865–942 (2009). URL <https://link.aps.org/doi/10.1103/RevModPhys.81.865>.

[3] Bennett, C. H. & DiVincenzo, D. P. Quantum information and computation. *nature* **404**, 247–255 (2000).

[4] Khalili, F. Y. & Polzik, E. S. Overcoming the standard quantum limit in gravitational wave detectors using spin systems with a negative effective mass. *Phys. Rev. Lett.* **121**, 031101 (2018). URL <https://link.aps.org/doi/10.1103/PhysRevLett.121.031101>.

[5] Zeuthen, E., Polzik, E. S. & Khalili, F. Y. Gravitational wave detection beyond the standard quantum limit using a negative-mass spin system and virtual rigidity. *Physical Review D* **100**, 062004 (2019).

[6] Ekert, A. K. Quantum cryptography based on bell’s theorem. *Phys. Rev. Lett.* **67**, 661–663 (1991). URL <https://link.aps.org/doi/10.1103/PhysRevLett.67.661>.

[7] Shor, P. W. & Preskill, J. Simple proof of security of the bb84 quantum key distribution protocol. *Physical review letters* **85**, 441 (2000).

[8] Gisin, N., Ribordy, G., Tittel, W. & Zbinden, H. Quantum cryptography. *Reviews of modern physics* **74**, 145 (2002).

[9] Bennett, C. H. Quantum information. *Physica Scripta* **1998**, 210 (1998).

[10] DiVincenzo, D. P. Quantum computation. *Science* **270**, 255–261 (1995).

[11] Steane, A. Quantum computing. *Reports on Progress in Physics* **61**, 117 (1998).

[12] DiVincenzo, D. P. The physical implementation of quantum computation. *Fortschritte der Physik: Progress of Physics* **48**, 771–783 (2000).

[13] Ladd, T. D. *et al.* Quantum computers. *nature* **464**, 45–53 (2010).

[14] Nielsen, M. A. & Chuang, I. L. *Quantum computation and quantum information* (Cambridge university press, 2010).

[15] Madsen, L. S. *et al.* Quantum computational advantage with a programmable photonic processor. *Nature* **606**, 75–81 (2022).

[16] Preskill, J. Quantum computing in the nisq era and beyond. *Quantum* **2**, 79 (2018).

[17] Riera-Sàbat, F., Sekatski, P. & Dür, W. Remotely controlled entanglement generation. *Quantum* **7**, 904 (2023).

[18] Zhang, Z. *et al.* Entanglement-based quantum information technology: a tutorial. *Advances in Optics and Photonics* **16**, 60–162 (2024).

[19] Wang, T.-L. *et al.* Remote entanglement generation via enhanced quantum state transfer. *arXiv preprint arXiv:2506.06669* (2025).

[20] Arute, F. *et al.* Quantum supremacy using a programmable superconducting processor. *Nature* **574**, 505–510 (2019).

[21] Cirac, J. I. & Zoller, P. Quantum computations with cold trapped ions. *Phys. Rev. Lett.* **74**, 4091–4094 (1995). URL <https://link.aps.org/doi/10.1103/PhysRevLett.74.4091>.

[22] Monroe, C. *et al.* Large-scale modular quantum-computer architecture with atomic memory and photonic interconnects. *Physical Review A* **89**, 022317 (2014).

[23] Zhong, H.-S. *et al.* Quantum computational advantage using photons. *Science* **370**, 1460–1463 (2020).

[24] Humphreys, P. C. *et al.* Deterministic delivery of remote entanglement on a quantum network. *Nature* **558**, 268–273 (2018).

[25] Tyryshkin, A. M. *et al.* Electron spin coherence exceeding seconds in high-purity silicon. *Nature materials* **11**, 143–147 (2012).

[26] Pla, J. J. *et al.* High-fidelity readout and control of a nuclear spin qubit in silicon. *Nature* **496**, 334–338 (2013).

[27] Watson, T. F. *et al.* A programmable two-qubit quantum processor in silicon. *nature* **555**, 633–637 (2018).

[28] Loss, D. & DiVincenzo, D. P. Quantum computation with quantum dots. *Phys. Rev. A* **57**, 120–126 (1998). URL <https://link.aps.org/doi/10.1103/PhysRevA.57.120>.

[29] Nowack, K. C., Koppens, F., Nazarov, Y. V. & Vandersypen, L. Coherent control of a single electron spin with electric fields. *Science* **318**, 1430–1433 (2007).

[30] Petta, J. R. *et al.* Coherent manipulation of coupled electron spins in semiconductor quantum dots. *Science* **309**, 2180–2184 (2005). Epub 2005 Sep 1.

[31] Zajac, D. M. *et al.* Resonantly driven cnot gate for electron spins. *Science* **359**, 439–442 (2018).

[32] Bluhm, H. *et al.* Dephasing time of gaas electron-spin qubits coupled to a nuclear bath exceeding 200 μ s. *Nature Physics* **7**, 109–113 (2011).

[33] Chen, S.-H. Origin and early growth of entanglement by *sd* exchange with gate voltage controllable outcome. *Phys. Rev. B* **109**, 045308 (2024). URL <https://link.aps.org/doi/10.1103/PhysRevB.109.045308>.

[34] Lin, L.-C., Tan, S. G., Chang, C.-R., Sun, S.-J. & Chen, S.-H. Entanglement induced by heisenberg exchange between an electron in a nested quantum dot and a qubit with relative motion. *New Journal of Physics* (2025).

[35] Vavilov, M. G. & Glazman, L. I. Transport spectroscopy of kondo quantum dots coupled by rkky interaction. *Phys. Rev. Lett.* **94**, 086805 (2005). URL <https://link.aps.org/doi/10.1103/PhysRevLett.94.086805>.

[36] Petersson, K. D. *et al.* Circuit quantum electrodynamics with a spin qubit. *Nature* **490**, 380–383 (2012).

[37] Yang, G., Hsu, C.-H., Stano, P., Klinovaja, J. & Loss, D. Long-distance entanglement of spin qubits via quantum hall edge states. *Phys. Rev. B* **93**, 075301 (2016). URL <https://link.aps.org/doi/10.1103/PhysRevB.93.075301>.

[38] Wang, J.-N. *et al.* Unified formulations for rkky interaction, side kondo behavior, and fano antiresonance in a hybrid tripartite quantum dot device with filtered density of states. *Phys. Rev. B* **106**, 035428 (2022). URL <https://link.aps.org/doi/10.1103/PhysRevB.106.035428>.

[39] Vonhoff, F., Fischer, A., Deltenre, K. & Anders, F. B. Microscopic origin of the effective spin-spin interaction in a semiconductor quantum dot ensemble. *Phys. Rev. Lett.* **129**, 167701 (2022). URL <https://link.aps.org/doi/10.1103/PhysRevLett.129.167701>.

[40] Utsumi, Y., Martinek, J., Bruno, P. & Imamura, H. Indirect exchange interaction between two quantum dots in an aharonov-bohm ring. *Physical Review B* **69**, 155320 (2004).

[41] Stocker, L. & Zilberberg, O. Coherent exchange-coupled nonlocal kondo impurities. *Physical Review Research* **6**, L022058 (2024).

[42] Chen, S.-H., Maekawa, S., Liu, M.-H. & Chang, C.-R. Mirror symmetry and exchange of magnetic impurities mediated by electrons of rashba spin–orbit interaction in a four-terminal landauer setup. *Journal of Physics D: Applied Physics* **43**, 015003 (2009).

[43] Allerdt, A., Büsser, C. A., Martins, G. B. & Feiguin, A. E. Kondo versus indirect exchange: Role of lattice and actual range of rkky interactions in real materials. *Phys. Rev. B* **91**, 085101 (2015). URL <https://link.aps.org/doi/10.1103/PhysRevB.91.085101>.

[44] Mousavi, F. M. & Farghadan, R. Electrical control of ruderman–kittel–kasuya–yosida exchange interaction in zigzag edge mos2 nanoflakes. *Journal of Physics and Chemistry of Solids* **158**, 110242 (2021).

[45] Kettemann, S. Competition between kondo effect and rkky coupling. *arXiv preprint arXiv:2408.03112* (2024).

[46] Ruderman, M. A. & Kittel, C. Indirect exchange coupling of nuclear magnetic moments by conduction electrons. *Phys. Rev.* **96**, 99 (1954).

[47] Kasuya, T. A theory of metallic ferro- and antiferromagnetism. *Progr. Theoret. Phys.* **16**, 45 (1956).

[48] Yosida, K. Magnetic properties of cu-mn alloys. *Phys. Rev.* **106**, 893 (1957).

[49] Cho, S. Y. & McKenzie, R. H. Quantum entanglement in the two-impurity kondo model. *Phys. Rev. A* **73**, 012109 (2006). URL <https://link.aps.org/doi/10.1103/PhysRevA.73.012109>.

[50] Elman, S. J., Bartlett, S. D. & Doherty, A. C. Long-range entanglement for spin qubits via quantum hall edge modes. *Phys. Rev. B* **96**, 115407 (2017). URL <https://link.aps.org/doi/10.1103/PhysRevB.96.115407>.

[51] Yu, T. & Eberly, J. H. Finite-time disentanglement via spontaneous emission. *Phys. Rev. Lett.* **93**, 140404 (2004). URL <https://link.aps.org/doi/10.1103/PhysRevLett.93.140404>.

[52] Yu, T. & Eberly, J. Sudden death of entanglement: classical noise effects. *Optics Communications* **264**, 393–397 (2006).

[53] Yu, T. & Eberly, J. Quantum open system theory: bipartite aspects. *Physical review letters* **97**, 140403 (2006).

[54] Ann, K. & Jaeger, G. Local-dephasing-induced entanglement sudden death in two-component finite-dimensional systems. *Phys. Rev. A* **76**, 044101 (2007). URL <https://link.aps.org/doi/10.1103/PhysRevA.76.044101>.

[55] Yu, T. & Eberly, J. H. Sudden death of entanglement. *Science* **323**, 598–601 (2009).

[56] Yuan, X.-Z., Goan, H.-S. & Zhu, K.-D. Non-Markovian reduced dynamics and entanglement evolution of two coupled spins in a quantum spin environment. *Phys. Rev. B* **75**, 045331 (2007). URL <https://link.aps.org/doi/10.1103/PhysRevB.75.045331>.

[57] Wang, F. *et al.* Observation of entanglement sudden death and rebirth by controlling a solid-state spin bath. *Phys. Rev. B* **98**, 064306 (2018). URL <https://link.aps.org/doi/10.1103/PhysRevB.98.064306>.

[58] Chen, S.-H., Tan, S. G. & Huang, C.-C. General recipe for immediate entanglement death and birth via bell states: environmental heisenberg exchange with transition as an example. *Physica Scripta* **100**, 065114 (2025).

[59] Almeida, M. P. *et al.* Environment-induced sudden death of entanglement. *science* **316**, 579–582 (2007).

[60] Hutton, A. & Bose, S. Mediated entanglement and correlations in a star network of interacting spins. *Phys. Rev. A* **69**, 042312 (2004). URL <https://link.aps.org/doi/10.1103/PhysRevA.69.042312>.

[61] Bazhanov, D. I., Sivkov, I. N. & Stepnyuk, V. S. Engineering of entanglement and spin state transfer via quantum chains of atomic spins at large separations. *Scientific Reports* **8**, 14118 (2018).

[62] Stocker, L., Sack, S. H., Ferguson, M. S. & Zilberberg, O. Entanglement-based observables for quantum impurities. *Phys. Rev. Res.* **4**, 043177 (2022). URL <https://link.aps.org/doi/10.1103/PhysRevResearch.4.043177>.

[63] Mondal, P., Suresh, A. & Nikolić, B. K. When can localized spins interacting with conduction electrons in ferro- or antiferromagnets be described classically via

the landau-lifshitz equation: Transition from quantum many-body entangled to quantum-classical nonequilibrium states. *Phys. Rev. B* **104**, 214401 (2021). URL <https://link.aps.org/doi/10.1103/PhysRevB.104.214401>

[64] Garcia-Gaitan, F. & Nikolić, B. K. Fate of entanglement in magnetism under Lindbladian or non-Markovian dynamics and conditions for their transition to Landau-Lifshitz-Gilbert classical dynamics. *Phys. Rev. B* **109**, L180408 (2024). URL <https://link.aps.org/doi/10.1103/PhysRevB.109.L180408>.

[65] Mortezapour, A., Borji, M. A. & Franco, R. L. Protecting entanglement by adjusting the velocities of moving qubits inside non-markovian environments. *Laser Physics Letters* **14**, 055201 (2017).

[66] Huan, T., Zhou, R. & Ian, H. Dynamic entanglement transfer in a double-cavity optomechanical system. *Phys. Rev. A* **92**, 022301 (2015). URL <https://link.aps.org/doi/10.1103/PhysRevA.92.022301>.

[67] Obada, A. F., Hessian, H. & Hashem, M. Quantum entanglement in a system of two moving atoms interacting with a single mode field. *Physica Scripta* **81**, 055303 (2010).

[68] Pandit, M., Das, S., Roy, S. S., Dhar, H. S. & Sen, U. Effects of cavity-cavity interaction on the entanglement dynamics of a generalized double jaynes-cummings model. *Journal of Physics B: Atomic, Molecular and Optical Physics* **51**, 045501 (2018).

[69] Costa Jr, A. & Bose, S. Impurity scattering induced entanglement of ballistic electrons. *Physical review letters* **87**, 277901 (2001).

[70] Sharma, A. & Tulapurkar, A. A. Transmission-based tomography for spin qubits. *Physical Review A* **103**, 052430 (2021).

[71] Leon, A. O., d'Albuquerque e Castro, J., Retamal, J. C., Cahaya, A. B. & Altbir, D. Manipulation of the rkky exchange by voltages. *Phys. Rev. B* **100**, 014403 (2019). URL <https://link.aps.org/doi/10.1103/PhysRevB.100.014403>.

[72] Tran, B. X. *et al.* Field-free control and switching of perpendicular magnetization by voltage induced manipulation of rkky interaction. *Applied Physics Letters* **124** (2024).

[73] Trényi, R. *et al.* Activation of metrologically useful genuine multipartite entanglement. *New Journal of Physics* **26**, 023034 (2024).

[74] Hahn, E. L. Spin echoes. *Phys. Rev.* **80**, 580–594 (1950). URL <https://link.aps.org/doi/10.1103/PhysRev.80.580>.

[75] Yosida, K. Bound state due to the $s - d$ exchange interaction. *Phys. Rev.* **147**, 223–227 (1966). URL <https://link.aps.org/doi/10.1103/PhysRev.147.223>.

[76] Allerdt, A., Feiguin, A. E. & Das Sarma, S. Competition between kondo effect and rkky physics in graphene magnetism. *Phys. Rev. B* **95**, 104402 (2017). URL <https://link.aps.org/doi/10.1103/PhysRevB.95.104402>.

[77] Doniach, S. The kondo lattice and weak antiferromagnetism. *Physica B+C* **91**, 231–234 (1977). URL <https://www.sciencedirect.com/science/article/pii/0378436377900021>.

[78] Kroha, J. Interplay of Kondo effect and RKKY interaction. In Pavarini, E., Koch, E., Scalettar, R. & Martin, R. M. (eds.) *The Physics of Correlated Insulators, Metals, and Superconductors Modeling and Simulation*, vol. 7 (Verlag des Forschungszentrum Jülich, 2017).

[79] Hill, S. A. & Wootters, W. K. Entanglement of a pair of quantum bits. *Phys. Rev. Lett.* **78**, 5022–5025 (1997). URL <https://link.aps.org/doi/10.1103/PhysRevLett.78.5022>.

[80] Wootters, W. K. Entanglement of formation of an arbitrary state of two qubits. *Phys. Rev. Lett.* **80**, 2245–2248 (1998). URL <https://link.aps.org/doi/10.1103/PhysRevLett.80.2245>.

[81] Rungta, P., Bužek, V., Caves, C. M., Hillery, M. & Milburn, G. J. Universal state inversion and concurrence in arbitrary dimensions. *Phys. Rev. A* **64**, 042315 (2001). URL <https://link.aps.org/doi/10.1103/PhysRevA.64.042315>.

[82] Walls, D. F. Squeezed states of light. *nature* **306**, 141–146 (1983).

[83] Wu, L.-A., Xiao, M. & Kimble, H. Squeezed states of light from an optical parametric oscillator. *Journal of the Optical Society of America B* **4**, 1465–1475 (1987).

[84] Pirkkalainen, J.-M., Damskägg, E., Brandt, M., Massel, F. & Sillanpää, M. A. Squeezing of quantum noise of motion in a micromechanical resonator. *Phys. Rev. Lett.* **115**, 243601 (2015). URL <https://link.aps.org/doi/10.1103/PhysRevLett.115.243601>.

[85] Marti, S. *et al.* Quantum squeezing in a nonlinear mechanical oscillator. *Nature Physics* **20**, 1448–1453 (2024).